New dynamic model for multimode chirp in DFB semiconductor lasers

A.J. Lowery, PhD, MIEE

Indexing terms: Semiconductor lasers, Modelling

Abstract: A new technique for modelling the dynamic spectral characteristics of DFB semiconductor lasers above threshold, which is based on the transmission-line laser model, is described. This includes the effects of index carrier dependence and longitudinal index variations. The time-domain responses and spectra of quarter-wave shifted grating devices are compared with unshifted devices under transient conditions.

1 Introduction

Distributed feedback (DFB) semiconductor lasers offer improved spectral characteristics over Fabry-Perot devices because of the use of a frequency selective grating over their length (Fig. 1). Their ability to remain in a single-longitudinal-mode while under modulation (dynamic single-mode: DSM) reduces pulse dispersion in long-haul fibre-optic communications systems. This allows higher data rates than with Fabry-Perot sources. However, dynamic single-mode operation is difficult to achieve [1]. Even when single-mode operation is achieved, by careful design of the laser's structure, the spectrum is broadened by chirping [2–4], causing dispersion [5].

Although models are available to predict the steady-state spectra of DFB lasers [6–8], few have been extended to dynamic operation. Hemni *et al.* have studied the effects of multimode oscillation in optical systems including modulated DFB lasers [9]. However, laser chirp was not considered. Bickers and Westbrook have modelled chirp using a simple, single-mode rate-equation approach [10]. However, longitudinal inhomogeneities were not considered. Kinoshita and Matsumoto modelled transient chirping and included longitudinal hole burning [11]. However, their model assumed that the device oscillated in a single longitudinal mode.

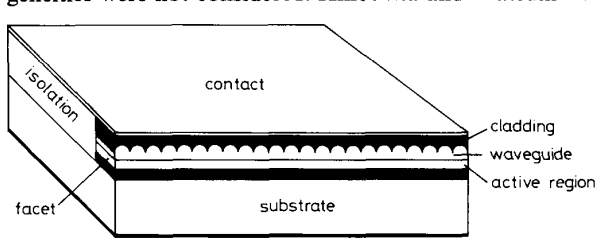

Fig. 1 *Typical DFB structure, bisected along the active region to show grating structure*

Paper 7407J (E13), first received 15th November 1989 and in revised form 14th March 1990

The author was formerly with the Department of Electrical and Electronic Engineering, University of Nottingham, Nottingham NG7 2RD, United Kingdom and is now with the Department of Electrical and Electronic Engineering, University of Melbourne, Parkville, Victoria 3052, Australia

Ideally, any dynamic model should include both chirping *and* multiple modes. This would allow the dispersion penalities caused by both spectral broadening mechanisms to be assessed. This paper presents such a model, which is based on a previously described scattering matrix approach [12] and is one of a family of laser models called transmission-line laser models (TLLMs) [13–17].

Transmission-line laser models split the laser cavity longitudinally into a number of sections. Each section contains a centrally placed scattering matrix which modifies forward and backward travelling waves on transmission lines which connect the matrices. Iteration in the time-domain gives the output wave from which spectra are found using Fourier transforms.

Unlike transfer-matrix models, which are solved in the frequency domain [18, 19, 6], TLLMs are suitable for dynamic simulations. Also, because the time evolutions of both the optical field and the carrier density are solved together, the models easily cope with gain saturation caused by carrier depletion [6].

The model may be applied to multicontact lasers, such as phase-tunable lasers [20], tunable lasers [21, 22], and lasers designed to compensate for spatial hole burning [23]. The model may also be applicable to tunable DFB laser amplifiers [24], the noise properties of DFB laser amplifiers [19] and to bistable DFB switches [25].

2 Model theory

Much of the model's theory exists already. This is because the TLLM already has been applied to DFB lasers without chirp [12] in a model derived from a Fabry-Perot laser model [13]. As with all TLLMs, the model is based on the transmission-line modelling (TLM) method, which uses transmission lines as an intermediate model between reality and a computer algorithm [26].

A simple TLM consists of two repeated operations; scattering and connecting. These modify voltage pulses travelling between scattering nodes on transmission lines. The scattering operation takes voltage pulses incident on the nodes ${}_kV^i$, and scatters them to give voltage pulses reflected from the nodes, ${}_kV^r$. It can be written as a scattering matrix, $\boldsymbol{S}$, operating on vectors $\boldsymbol{V}$, i.e.

$$ {}_kV^r = \boldsymbol{S} \cdot {}_kV^i \tag{1} $$

where k is the iteration number.

The scattering operation can be derived from a knowledge of the impedances of the transmission lines and associated components, such as resistors, at the nodes. It

may also include source terms, V^s so that

$$ {}_kV^r = S \cdot {}_kV^i + {}_kV^s \quad (2) $$

The connection operation describes how the reflected pulses propagate between scattering nodes to become new incident pulses for the next scattering operation. Again, it can be written as a matrix operation,

$$ {}_{k+1}V^i = C \cdot {}_kV^r \quad (3) $$

The connection matrix can be derived from the topology of the network and is usually very sparse as only adjacent nodes are connected. Note that the transmission lines must have equal delays, equal to the iteration timestep ΔT so that all pulses arrive at the nodes in synchronism.

The numerical computation consists of initialising the value of vector V^i and then repeating eqns. 2 and 3 to find the time evolution of the vector V^i or the vector V^r. In most cases, however, the required output quantity is a function of one of these vectors.

In transmission-line *laser* models, the voltage pulses represent the optical fields along the cavity. A chain of transmission lines form a one-dimensional model of the optical cavity, from facet to facet. The scattering matrices represent the optical process of stimulated emission, spontaneous emission and attenuation. A rate equation model of the local carrier density sets the magnitudes of these processes at a particular matrix.

Such a model has been used to simulate Fabry-Perot lasers [13–15], external-cavity lasers [16] and mode-locked lasers [17]. The addition of external interfaces has allowed laser amplifiers to be studied [27–29].

The DFB model, presented in Reference 12, used modified connection matrices to represent cross-coupling between the forwards and backwards travelling waves. However, because the delays of the transmission line have to be constant, index changes, causing chirping, could not be modelled.

The problem of chirping in Fabry-Perot TLLMs was solved by placing variable impedance stub extensions at the ends of the laser cavity [15]. These served to alter the phase-length of the cavity over a limited bandwidth. The stubs were placed at the cavity ends, rather than along the entire cavity length, to prevent midcavity coupling between the forward and backward travelling waves. This intracavity coupling would be a result of the impedance discontinuities caused by the stubs. Such coupling was found to make the Fabry-Perot laser model behave like a DFB laser model [30].

A new approach is introduced in this paper. Instead of connecting the stubs in series with the transmission lines modelling the cavity (Fig. 2*a*), circulators are used (Fig. 2*b*). These send the waves, out of the stubs, in the correct direction. For example, a forward wave will enter the first, left-hand, circulator (port 1) and be directed to the stub port (port 2). Because the stub presents an impedance mismatch, part off the wave will be reflected back into port 2. The circulator then directs this reflected wave to port 3, where it continues on as a forward wave. The remainder of the wave enters the stub to be delayed before returning to port 2 to be directed to port 3.

Backward waves simply pass from port 3 to port 1 of this first circulator. A second set of three-port circulators is used to delay the backward waves. This offers the possibility of having a direction-dependent index, as used in optical isolators.

The phase delay caused by the stubs is varied by altering their impedance. For example, an infinite stub impedance gives a reflection with zero phase shift; a matched capacitive stub gives a phase shift of $(2\pi \cdot \Delta T \cdot f)$ radians; a zero impedance stub gives π radians; a matched inductive (shorted) stub gives $(-2\pi \cdot \Delta T \cdot f)$ radians, where f is the optical frequency. Other phase shifts are available, over a limited bandwidth, by using other reflection coefficients.

A complete DFB model is shown in Fig. 3. Here, scattering matrices have been inserted between the circulators of each section. Also, alternate sections' transmission-lines have different impedances. This creates impedance mismatches at the section boundaries, which couple the forward and backward waves [12]. Each section has an associated carrier rate equation model to enable the local gain, refractive index and spontaneous noise to be calculated from the injection current and the carrier recombination rates [13].

If two sections of the model were to be used to represent each period of the DFB grating on the real device, the number of sections and hence the computational task would be excessive. However, it is possible to represent

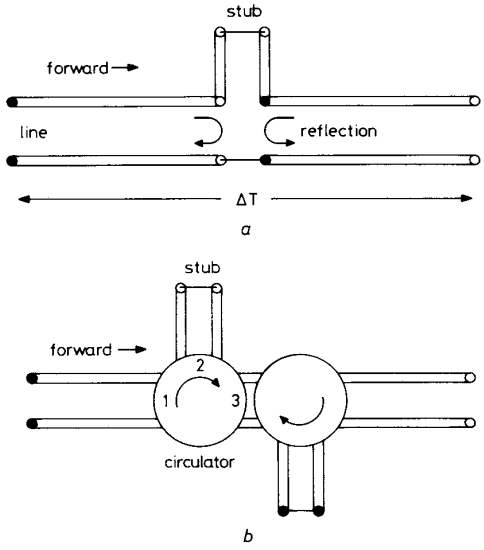

Fig. 2 *Two methods of adding phase delays to TLM models*

a Using a stub directly connected to the lines
b Using circulators and separate stubs for the forward and backward waves

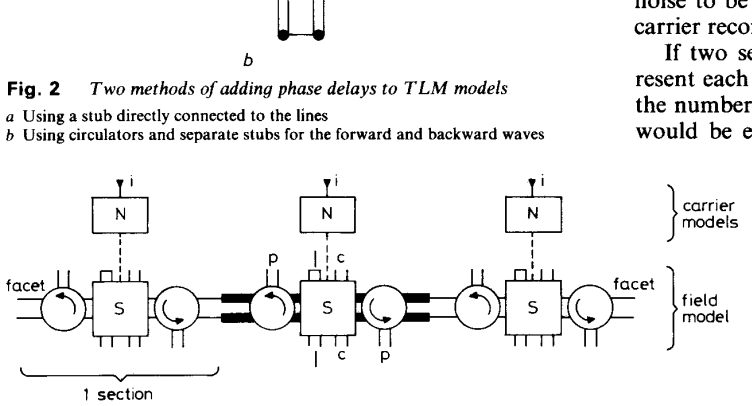

Fig. 3 *Complete DFB laser model*

p is a phase-shift stub, *l* and *c* are gain-filter stubs, *i* = injection current

an odd number of grating periods with a single pair of model sections without compromising the model's accuracy [12]. This technique relies on the model having a 'square' grating modulation. This can be decomposed into a number of sinusoidal gratings at harmonics of the grating period by Fourier techniques. One of these harmonics models the real device's grating period.

Note that the amplitude of each harmonic decreases with the harmonic number, e.g. the fifth harmonic produces a coupling of one-fifth of the amplitude of the fundamental. For this example, the coupling of each period of the square grating has to be increased by a factor of five over the coupling of the real laser's grating to compensate. A simpler and much neater rule is that the coupling κ per unit length must be equal for model and real devices [12].

If a small number of sections is used, the optical field will be sampled less than once per wave period. This undersampling is essential for realistic computer times. Undersampling has been used in all TLLMs and does not compromise accuracy if the sampling rate (section length/group velocity) is more than twice the bandwidth of the optical wave [13]. The use of two sections per grating period ensures that the DFB's spectrum always lies near the centre of the modelled spectrum.

3 Derivation of the algorithm from the transmission-line model

Once the transmission line representation of the device has been derived, an algorithm can be produced. One of the advantages of TLM is that the algorithm is always an exact representation of the transmission-line model; no inaccuracies are introduced once the transmission-line representation has been formulated. This means that all approximations have physical meaning because they are associated with the parameters of the transmission lines.

The terms in eqns. 1 to 3 will now be derived for the DFB laser model. Note that the travelling optical fields (electric fields) are represented by voltage pulses A (forwards) and B (backwards) in the model. Thus, a unity constant m, with dimensions of metres, is used to convert between electric field and voltage to maintain dimensional correctness.

3.1 Scattering matrices, S

The scattering matrix can be split into two scattering matrices; one for each wave direction. This is possible as there is no cross-coupling between the wave directions in the scattering operation. Scattering matrices for a cavity without phase shifting elements were derived in Reference 32. These have been extended to include the circulators and stubs by consideration of the reflections at the stub-cavity interfaces. The scattering process for the forward wave, with incident pulses from the previous section $A^i(n)$, the gain filter's capacitive stub $A^i_C(n)$, the gain filter's inductive stub $A^i_L(n)$ and the phase shifting stub $A^i_P(n)$, is

$$\begin{bmatrix} A(n) \\ A_C(n) \\ A_L(n) \\ A_P(n) \end{bmatrix}^r = \frac{1}{y(1+Z_s)} \begin{bmatrix} t(g+y)(Z_s-1) & 2tY_C(Z_s-1) & 2tY_L(Z_s-1) & 2y \\ g(Z_s+1) & (2Y_C-y)(Z_s+1) & 2Y_L(Z_s+1) & 0 \\ g(Z_s+1) & 2Y_C(Z_s+1) & (2Y_L-y)(Z_s+1) & 0 \\ t(g+y)2Z_s & 4tY_CZ_s & 4tY_LZ_s & y(1-Z_s) \end{bmatrix}_k \begin{bmatrix} A(n) \\ A_C(n) \\ A_L(n) \\ A_P(n) \end{bmatrix}_k^i + \begin{bmatrix} (Z_s-1)\cdot I_sZ_pt/2 \\ 0 \\ 0 \\ Z_sI_sZ_pt \end{bmatrix}_k^s \quad (4)$$

The scattering process for the backward wave is simply the above formula with all wave amplitudes A replaced by wave amplitudes B.

The terms within this matrix have been derived previously [32], but will be repeated here for clarity. Note that all the terms may vary from section to section and, therefore, should technically have subscripts n. Also, some terms are time-dependent and vary with the iteration number k.

The spectral dependence of the gain is modelled using transmission-line stub filters [13]. The sum of the gain-curve filter's stub admittances y, is

$$y = 1 + Y_L + Y_C \quad (5)$$

The stubs' admittances Y_C (capacitive) and Y_L (inductive) are given in Reference 13.

The field gain, resulting from stimulated emission, across a section of length ΔL is

$$g = \exp\left[a\,\Delta L\Gamma(N(n) - N_0)/2\right] \rightarrow 1 \quad (6)$$

where a is the gain cross-section, Γ is the confinement factor, $N(n)$ is the carrier concentration within section n and N_0 is the carrier density for transparency.

The attenuation, caused by free-carrier absorption and scattering, across a section is

$$t = \exp\left(-\alpha_{sc}\,\Delta L/2\right) \quad (7)$$

where α_{sc} is the attenuation per unit length.

Spontaneous emission is modelled with a filtered Gaussian (normal) distribution noise current I_s with a mean-square value of [14]

$$\langle I_s^2 \rangle = 2\beta LhfB[N(n)]^2m^2/Z_p \quad (8)$$

where β is the spontaneous emission coupling coefficient, L is the laser's cavity length, hf is the photon energy, B is the bimolecular (radiative) recombination coefficient, m is a unit constant with dimensions of metres and Z_p is the cavity wave impedance [13].

The phase-adjusting stub's impedances Z_s are normalised to the cavity wave impedance and are given by

$$Z_s = |\cot(\pi f l\bar{n}_e/c)| \quad (9)$$

and l is the change in phase length across a section such that

$$l = \Gamma\frac{\Delta L}{\bar{n}_e}[N(n) - N_P]\,dn/dN \quad (10)$$

where N_P is an arbitrary carrier concentration for zero phase shift and is usually set to the threshold carrier density [15], $\bar{n}_e$ is the guide's group effective index (equal to the effective index in this dispersionless model) and c is the velocity of light in a vacuum.

The active region's carrier index dependence dn/dN can be related to Henry's α factor by

$$\frac{dn}{dN} = -\frac{\alpha ca}{4\pi f} \quad (11)$$

3.2 Connection equations (**C** for the link-lines between sections)

The connection equations in TLLM DFB models describe the cross-coupling between the two wave directions occurring at the section interfaces. They were derived in Reference 12 and are used alternately along the laser model. They are

$$ {}_{k+1}\begin{bmatrix} A(n+1) \\ B(n) \end{bmatrix}^i = \begin{bmatrix} 1+\kappa\,\Delta L & -\kappa\,\Delta L \\ \kappa\,\Delta L & 1-\kappa\,\Delta L \end{bmatrix} \times {}_{k}\begin{bmatrix} A(n) \\ B(n+1) \end{bmatrix}^r \quad (12) $$

for a low-high impedance boundary and

$$ {}_{k+1}\begin{bmatrix} A(n+2) \\ B(n+1) \end{bmatrix}^i = \begin{bmatrix} 1-\kappa\,\Delta L & \kappa\,\Delta L \\ -\kappa\,\Delta L & 1+\kappa\,\Delta L \end{bmatrix} \times {}_{k}\begin{bmatrix} A(n+1) \\ B(n+2) \end{bmatrix}^r \quad (13) $$

for a high-low impedance boundary κ, ΔL is the grating coupling per unit length for the device multiplied by the length of one modelling section.

For a standard DFB device (e.g. Reference 2), eqns. 2 and 3 are applied alternately along the device length, i.e. $n = (1, 3, 5, 7, \ldots)$. For quarter-wave shifted grating devices (e.g. Reference 31), a zero reflection interface (identity matrix) is inserted half way along the cavity.

There may also be coupling at the facets. For facets placed at a low-high impedance boundary a simple resistive termination can be used giving

$$ {}_{k+1}B^i(s) = \sqrt{(R)} \cdot {}_kA^r(s) \quad \text{at the front facet} $$
$$ {}_{k+1}A^i(1) = \sqrt{(R)} \cdot {}_kB^r(1) \quad \text{at the rear facet} \quad (14) $$

where R is the power reflectivity of the facets [13], and s is the number of sections.

A more complex model, including phase-shifting stubs between the facets and the cavity, could be used to model the effects of facet phase on mode-stability [33].

3.3 Connection equations **C** for the stubs within a section)

There are also equations governing the reflections at the ends of the transmission line stubs. These are half a time-step long to ensure that pulses arrive back at the originating scattering matrix after a delay of one timestep.

For the inductive stubs in each section the reflection coefficient is negative, giving

$$ {}_{k+1}A^i_L(n) = -{}_kA^r_L(n) $$
$$ {}_{k+1}B^i_L(n) = -{}_kB^r_L(n) \quad (15) $$

For the capacitive stubs in each section the reflection coefficient is positive, giving

$$ {}_{k+1}A^i_C(n) = {}_kA^r_C(n) $$
$$ {}_{k+1}B^i_C(n) = {}_kB^r_C(n) \quad (16) $$

For the phase-adjusting stubs, which may be inductive or capacitive,

$$ {}_{k+1}A^i_P(n) = -{}_kA^r_P(n) $$
$$ {}_{k+1}B^i_P(n) = -{}_kB^r_P(n) $$

when the cotangent in eqn. 9 is negative

or

$$ {}_{k+1}A^i_P(n) = {}_kA^r_P(n) $$
$$ {}_{k+1}B^i_P(n) = {}_kB^r_P(n) $$

when the cotangent in eqn. 9 is positive (17)

3.4 Carrier density rate equation

If we assume that diffusion along the cavity is negligible, then independent carrier density rate equations may be used for each section of the model. This is a refinement over most laser models, which use a single carrier density rate equation to describe the density averaged over all the cavity. These may not be accurate for lasers with low-reflectivity facets, including laser amplifiers.

The rate equation for carrier density can be written

$$ \frac{dN(n)}{dt} = -AN(n) - B[N(n)]^2 - C[N(n)]^3 - \frac{ac\Gamma}{\bar{n}_e}(N(n) - N_0)S(n) + \frac{I(n)}{wd\,\Delta L q} \quad (18) $$

where A, B and C are the monomolecular, bimolecular and Auger recombination coefficients [34], respectively, wd is the cross-sectional area of the active region, q is the electronic charge and $I(n)$ is the component of injection current injected into section n. The photon density, $S(n)$, within a section is related to the incident waves from either side by

$$ S(n) = ([A^i(n)]^2 + [B^i(n)]^2)\bar{n}_e/(hfcZ_p m^2) \quad (19) $$

3.5 Output power

The power exiting the front facet P, is related to the wave incident on the facet from the cavity, $A^r(s)$ and the facet's power reflectivity R, by [13]

$$ P = [A^r(s)]^2(1-R)wd/(Z_p m^2) \quad (20) $$

This power is usually averaged over a number of iterations to remove high frequency components.

4 Simulations of DFB devices

The following numerical results serve to test the validity of the model and then to illustrate its value. A 1550 nm device was modelled [2]. Its parameters are given in Table 1 and were obtained from References 2, 34 and 35. Note that the combination of bandnumber and number of sections gives a central wavelength of 1632.65 nm. However, this restriction could be eased by modification of the algorithm.

Table 1: Laser parameters

Symbol	Parameter name	Value	Unit
λ_0	Gain-peak wavelength	1630.65	nm
L	Laser cavity length	200	μm
w	Active region width	2	μm
d	Active region depth	0.15	μm
Γ	Optical confinement factor	0.3	
$\bar{n}_e$	Laser group effective index	4.2	
N_0	Transparency carrier density	9.0×10^{17}	cm^{-3}
a	Laser gain constant	2.7×10^{-16}	cm^2
α_{sc}	Cavity attenuation factor	0.0	cm^{-1}
R	Laser facet reflectivities	0.0	
A	Monomolecular recombination coefficient	1.0×10^8	s^{-1}
B	Bimolecular recombination coefficient	8.6×10^{-11}	$cm^3\,s^{-1}$
C	Auger recombination coeffficient	4.0×10^{-29}	$cm^6\,s^{-1}$
β	Spontaneous coupling factor	1×10^{-4}	
c	Vacuum velocity of light	3×10^{10}	$cm\,s^{-1}$
s	Number of model sections	98	
b	Model bandnumber [13]	5	
κ	Grating coupling per unit length	160	cm^{-1}
I	Laser drive current	100	mA
N_i	Initial carrier density	1.5×10^{18}	cm^{-3}
$\Delta\lambda$	Gain peak offset from bandcentre	−2.0	nm
Q	Gain filters' Q-factor	12	
α	Henry's alpha factor	5.2	

4.1 Effect of number of model sections: devices without chirp

The validity of using a small number of sections for a large number of grating periods was tested by comparing the transmission responses of models with an increasing number of sections. The carrier concentration was fixed and an impulse injected into the rear facet. The impulse response, out of the front facet, was Fourier transformed to obtain the transmission spectrum.

Fig. 4 shows the transmission spectra for unshifted-DFB models with 23-, 96- and 392-sections and no phase-adjusting stubs operated just below threshold. Only a proportion of the bandwidths of the 98- and 392-section models were plotted to allow comparison with the response of the 23-section model. The responses of the 98- and 392-section models were in good agreement over the entire bandwidth of the 23-section model. The 23-section model's response was only a good fit over the stop-band. Thus, the 98 section model was thought to be a good compromise between accuracy and computational effort.

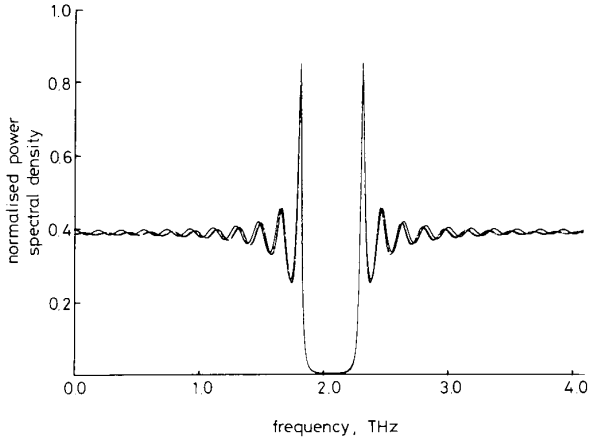

Fig. 4 *Transmission responses of 23- (solid-line), 98- and 960- (broken-line) section models with no stub phase shift, just below threshold*

4.2 Effect of number of model sections: devices with chirp

The validity of the phase-shifting stubs was checked by plotting the transmission response of a 23-section cavity with different amounts of static shift (Fig. 5*a*). The test was then repeated with a 98-section model (Fig. 5*b*).

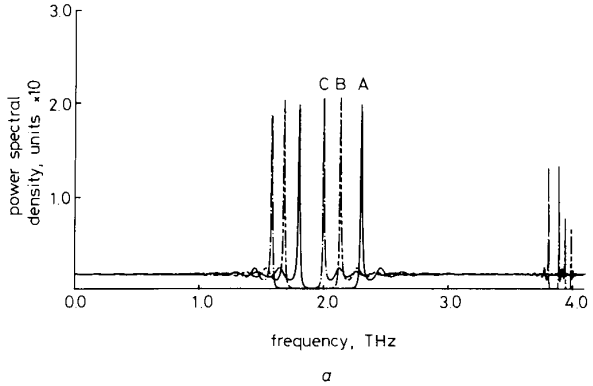

a

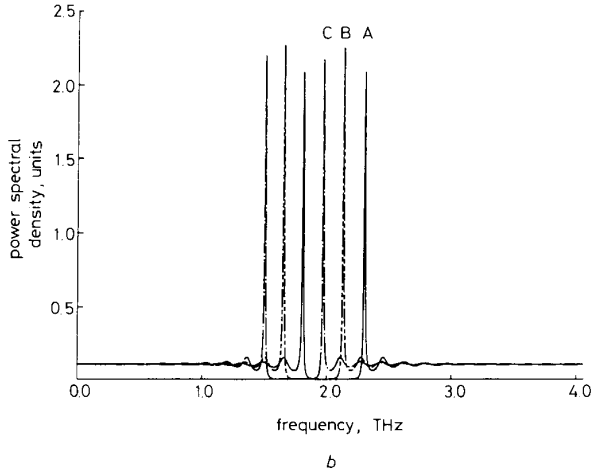

b

Fig. 5 *Transmission responses 23- and 98-section model*

a 23-section model just below threshold
- A no phase shift
- B -2.4×10^{17} cm^{-3} shift in carrier density
- C -4.8×10^{17} cm^{-3} shift in carrier density

b 98-section model (centre of band shown)
- A no phase shift
- B -2.4×10^{17} cm^{-3} shift in carrier density
- C -4.8×10^{17} cm^{-3} shift in carrier density

Examination of Fig. 5*a* shows that the transmission peaks are indeed shifted by altering the impedance of the phase stubs. Two unwanted effects occurred, however. The spacing between the two modes decreased with increasing shifts from the centre of the band. Secondly, when the modes were shifted down in frequency, other transmission peaks appeared at the top-end of the modelled bandwidth.

These effects were reduced in the 98-section model, with the disadvantage that the computation time was increased by a factor of about sixteen. Fig. 6 plots the error in the mode positions against the change in carrier concentration. Note that the error was symmetrical about the zero-shift position. This Figure can be used as a guide to the complexity of model required. It is not expected that the secondary modes appearing at the band edges will be a problem. This is because the gain-spectrum model will filter these out [13].

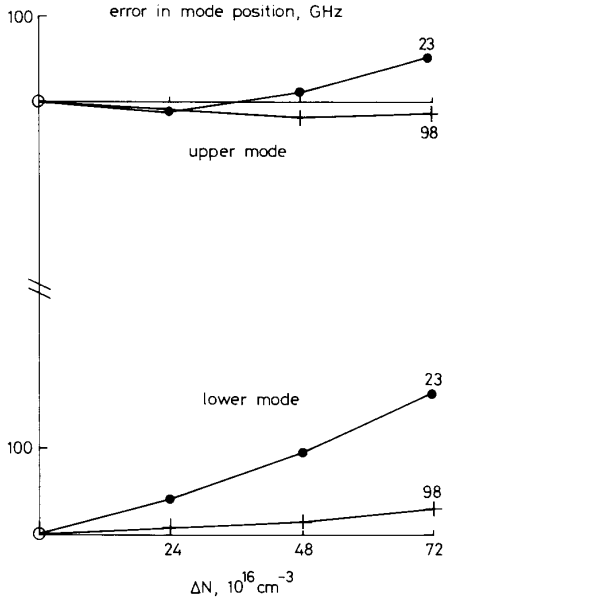

Fig. 6 *Error in mode positions against the carrier density deviation from N_P for the 23- and 98-section models*

4.3 Nonshifted DFB laser transient response

Many DFB models assume that the refractive index is constant along the cavity. However, if there is gain saturation along the cavity's length, the index will also be position dependent. Two simulations were used to investigate the effects of inhomogeneous index. The first assumed a homogeneous index, governed by the average carrier concentration within the cavity. In the second, the index in each section was fixed by the carrier concentration within that section.

In both simulations, the laser was subject to a step increase in injection current to 100 mA. This large value was used to induce length-dependent saturation and also to give short pulses and hence large spectral widths.

Fig. 7*a* shows the transient responses of a laser with a homogeneous index. This shows a classic damped relaxation oscillation, common to all lasers. Fig. 7*b* shows the spectra of the first and second pulses in Fig. 7*a*. The first pulse's spectrum (solid line) had an average width of 170 GHz for each mode.

The first pulse's width was 12.5 ps. This gives a time-bandwidth product of 2.12, less than the value of 2.33 given by the formula for Gaussian pulses, which has been shown to be a good approximation for Fabry-Perot lasers [15]. However, because of the asymmetry of the DFB spectra, it is difficult to define their FWHM width accurately. Note that this asymmetry, in particular the prominence of the red 'rabbit-ear', is common to experimental observations [2, 3, 5, 9].

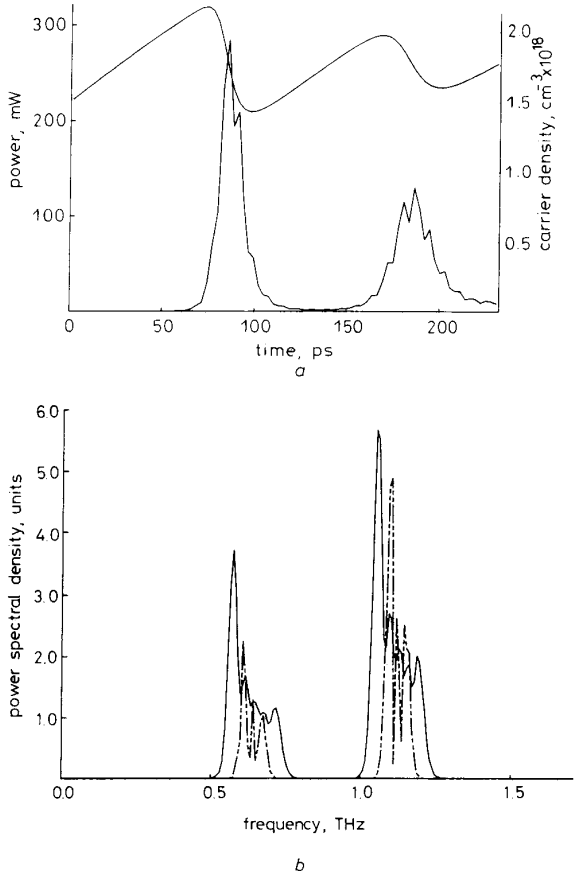

Fig. 7 *Transient response of DFB laser and spectra of first and second pulses*

a Transient response assuming homogeneous refractive index
b Spectra of first (solid) and second pulses (broken) (multiply PSD scale by 2 for second spectrum)

The model was re-run without including index variations to see whether homogeneous index variations had any effect on the temporal responses of lasers. Only small differences in the responses were observed. These could be explained by phase shifts between the power envelope and the averaging routine.

Fig. 8*a* shows the response of a laser allowing an inhomogeneous refractive index. Although the first pulses are similar, there are noticeable differences between this and the response using the homogeneous approximation. The differences included a lower threshold carrier density, a greater damping and a smoother response. The first pulses were expected to be similar because of the absence of gain saturation in these early times.

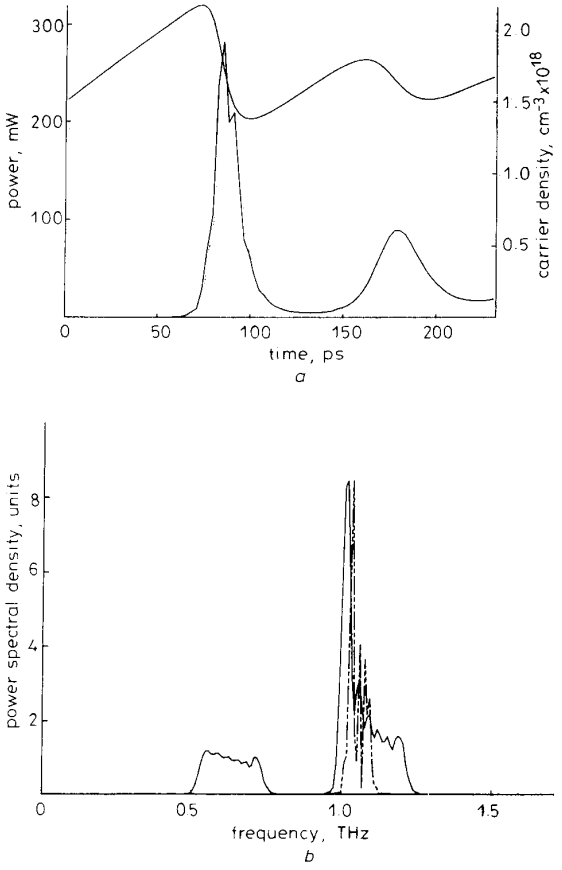

Fig. 8 *Transient response of DFB laser and spectra of first and second pulses*

a Transient response allowing inhomogeneous index
b Spectra of first and second pulses (multiply PSD scale by 2.5 for second spectrum)

Fig. 8*b* shows the spectra of the first and second pulses in Fig. 8*a*. The first pulse's spectrum had an average mode-width of 210 GHz. The first pulse's width was 11.4 ps, giving a time-bandwidth product of 2.4, closer to that of Fabry-Perot lasers. Note that the laser has settled to a single mode for the second pulse. This explains the smooth profile of the time-response.

The second pulse's spectrum is not centred on the first pulse's spectrum, but is shifted to the red. This is in agreement with the lower value of average carrier concentration than in the homogeneous simulations. This effect was observed in Reference 3, but was explained by junction heating. This effect would have important system consequences [36, 37].

4.5 Quarter-wave shifted laser transient response

Quarter-wave shifted DFB structures have a single, dominant oscillating mode. In contrast, unshifted devices usually support two modes, unless the facet reflectivities and phases are carefully chosen [31]. Thus, shifted DFB lasers are favoured in communications systems.

It is easy to modify the TLLM for quarter-wave shifted DFB lasers. The order of the low and high impedance sections is reversed in the middle of the model to give two adjacent sections of the same impedance.

Fig. 9*a* shows the transient response of a quarter-wave shifted device subject to the same drive conditions as before. As observed in Reference 12, the damping of the transient is better than for the unshifted device. Also, the carrier density settles to a lower level than for the unshifted devices.

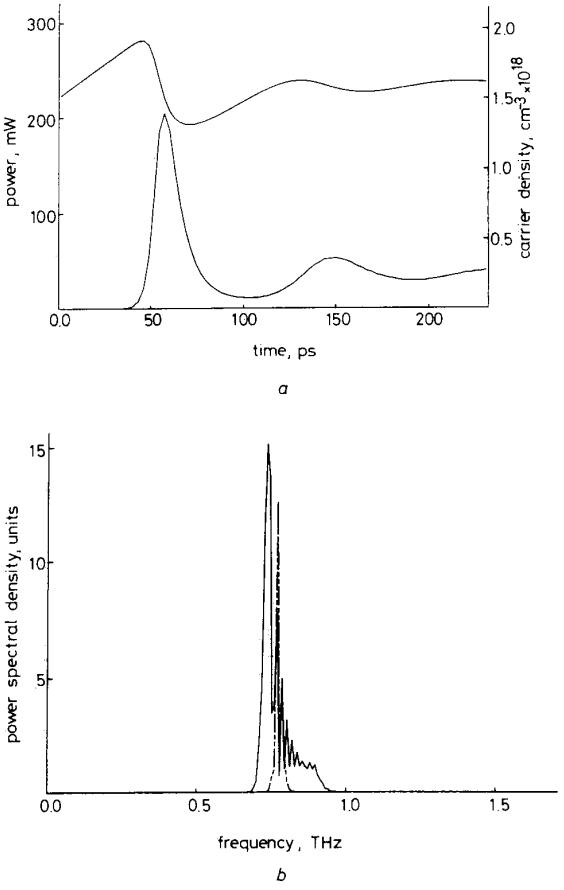

Fig. 9 *Transient response of DFB laser and spectra of first and second pulses*

a Transient response for quarter-wave shifted DFB laser
b Spectra of first and second pulses (multiply PSD scale by 4 for second spectrum)

The spectra of the two pulses in Fig. 9*a* are shown in Fig. 9*b*. As expected, a single mode dominates. The width of the first pulse's spectrum was 205 GHz with a corresponding temporal width of 15.6 ps. Thus, the time-bandwidth product was 3.2. The spectrum again shows a predominance of the red rabbit-ear, more so than in the unshifted device. Because this ear dominates the spectrum, the spectrum appears to shift to the blue as the relaxation oscillations settle. This is in agreement with Reference 11.

The oscillation in the power-spectral density is probably a result of interference between the main body of the pulse (carrier concentration falling) and the tail of the pulse (carrier concentration rising). This interference is enhanced by the increased damping giving more power in the pulse's tail. The second transform gives a very narrow spectrum, corresponding to the wide second pulse. Again, this lies to the red side of the centre of the first spectrum.

Further simulations, using a different amount of static phase shift (by altering N_P) showed that the model was still valid, even though the centre wavelength had been shifted. This means that the form of the spectra are nearly independent of the central wavelength in relation to the model's centre wavelength, as expected. If the number of sections were to be reduced, then some differences might be seen.

5 Conclusions

A new numerical modelling method for DFB lasers has been developed. This is based on a transmission-line laser model with cross-coupling between the forward and backward travelling waves and phase-shifting stubs coupled to the cavity using circulators.

Results from the model show that it is important to consider longitudinal variations in refractive index as these affect both the temporal and the spectral behaviour of DFBs. The modelled transient spectra were in good agreement with experimental results and show the highly asymmetric nature of DFB spectra.

One of the important qualities of numerical models is that they should allow results to be gained faster than from experimental work. Certainly this model allows parameters to be adjusted more quickly than in real devices. The simulation times were of the order of 40 min on a 32016-based machine (approx. 3× an 8 MHz IBM-AT). However, these can be reduced by compromising accuracy. This is simply achieved by reducing the number of model sections; halving the number of sections cuts the computational task by 75%. Also, current work aims to implement the algorithm on a multiprocessor machine with one section per processor.

The modelling method is extremely flexible as it is based on a building-block approach; each scattering matrix being a block. The model has been demonstrated on unshifted and quarter-wave DFB lasers. However, simple modifications to the injection-current profile would allow multicontact DFB lasers and a distributed Bragg reflector (DBR) to be simulated. Interesting experiments include the effect of drive pulse-shape on dynamic linewidth, the tuning speed of multicontact devices, a comparison between DFB and DBR lasers and the optimisation of the grating coupling coefficient.

The building blocks can be extended beyond the laser to allow more complex lasers and even optical systems to be modelled. For example, the DFB laser could be included within an external cavity to form a tuning element in a mode-locked laser. Alternatively, the model could be combined with a time-domain fibre model to calculate the dispersion penalty in long-haul systems. Also, the model can accept external inputs. This would allow DFB laser amplifiers, useful as wavelength selectors, to be optimised.

6 References

1 SASAKI, S., CHOY, M.M., and CHEUNG, N.K.: 'Effects of dynamic spectral behaviour and mode-partitioning of 1550 nm distributed feedback lasers on Gbit/s transmission systems', *Electron. Lett.*, 1988, **24**, pp. 26–28

2 WESTBROOK, L.D., HENNING, I.D., NELSON, A.W., and FIDDYMENT, P.J.: 'Spectral properties of strongly coupled 1.5 μm DFB laser diodes', *IEEE J.*, 1985, **QE-21,** pp. 512–518

3 BERGANO, N.S.: 'Wavelength discriminator method for measuring dynamic chirp in DFB lasers', *Electron. Lett.*, 1988, **24,** pp. 1296–1297

4 EISENSTEIN, G., TUCKER, R.S., and RAYBON, G.: 'Optical time-division multiplexed transmission at 8 Gbit/s using single laser and semiconductor optical power amplifier', *Electron. Lett.*, 1989, **25,** pp. 1034–1036

5 YAMAMOTO, S., KUWAZURU, M., WAKABAYASHI, H., and IWAMOTO, Y.: 'Analysis of chirp power penalty in 1.55 μm DFB-LD high-speed optical fiber transmission systems', *IEEE J.*, 1987, **LT-5,** pp. 1518–1524

6 WHITEAWAY, J.E., THOMPSON, G.H.B., COLLAR, A.J., ARMISTEAD, C.J.: 'The design and assessment of $\lambda/4$ phase-shifted DFB laser structures', *IEEE J.*, 1989, **QE-25,** pp. 1261–1279

7 SODA, H., KOTAKI, Y., SUDO, H., ISHIKAWA, H., YAMAKOSHI, S., and IMAI, H.: 'Stability in single longitudinal mode operation in GaInAsP/InP phase-adjusted DFB lasers', *IEEE J.*, 1987, **QE-23,** pp. 804–814

8 McCALL, S.L., and PLATZMAN, P.M.: 'An optimized $\pi/2$ distributed feedback laser', *IEEE J.*, 1985, **QE-21,** pp. 1899–1904

9 HEMNI, H., KOIZUMU, Y., YAMAGUCHI, M., SHIKADA, M., and MITO, I.: 'The influence of directly modulated DFB LD submode oscillation on long-span transmission system', *IEEE J.*, 1988, **LT-6,** pp. 636–642

10 BICKERS, L., and WESTBROOK, L.D.: 'Reduction of transient laser chirp in 1.5 μm DFB lasers by shaping the modulation pulse', *IEE Proc. J, Optoelectron.*, 1986, **133,** pp. 155–162

11 KINOSHITA, J-I., and MATSUMOTO, K.: 'Transient chirping in distributed feedback lasers: Effect of spatial hole-burning along the laser axis', *IEEE J.*, 1988, **QE-24,** pp. 2160–2169

12 LOWERY, A.J.: 'Dynamic modelling of distributed-feedback lasers using scattering matrices', *Electron. Lett.*, 1989, **25,** pp. 1307–1308

13 LOWERY, A.J.: 'A new dynamic semiconductor laser model based on the transmission line modelling method', *IEE Proc. J, Optoelectron.*, 1987, **134,** pp. 281–289

14 LOWERY, A.J.: 'A new time-domain model for spontaneous emission in semiconductor lasers and its use in predicting their transient response', *Int. J. Numerical Modelling*, 1988, **1,** pp. 153–164

15 LOWERY, A.J.: 'A model for picosecond dynamic laser chirp based on the transmission line laser model', *IEE Proc. J, Optoelectron.*, 1988, **135,** pp. 126–132

16 LOWERY, A.J.: 'A new dynamic multimode model for external cavity semiconductor lasers', *IEE Proc. J, Optoelectron.*, 1989, **136,** pp. 229–237

17 LOWERY, A.J.: 'A new time-domain model for active mode-locking based on the transmission-line laser model', *IEE Proc. J, Optoelectron.*, 1989, **136,** pp. 264–272

18 BJORK, G., and NILSSON, O.: 'A new exact and efficient numerical matrix theory of complicated laser structures: Properties of asymmetric phase-shifted DFB lasers', *IEEE J.*, 1987, **LT-5,** pp. 140–146

19 MAKINO, T., and GLINSKI, J.: 'Transfer matrix analysis of the amplified spontaneous emission of DFB semiconductor laser amplifiers', *IEEE J.*, 1988, **QE-24,** pp. 1507–1518

20 MURATA, S., MITO, I., and KOBAYASHI, K.: 'Frequency modulation and spectral characteristics for a 1.5 μm phase-tunable DFB laser', *Electron. Lett.*, 1987, **23,** pp. 12–13

21 YOSHIKUNI, Y., OE, K., MOTOSUGI, G., and MATSUOKA, T.: 'Broad wavelength tuning under single-mode oscillation with a multi-electrode distributed feedback laser', *Electron. Lett.*, 1986, **22,** pp. 1153–1154

22 YOSHIKUNI, Y., and MOTOSUGI, G.: 'Multielectrode distributed feedback laser for pure frequency modulation and chirping suppressed amplitude modulation', *J. Lightwave Technology*, 1987, **5,** pp. 516–522

23 USAMI, M., and SHIGEYUKI, A.: 'Suppression of longitudinal spatial hole-burning effect in $\lambda/4$-shifted DFB lasers by non-uniform current distribution', *IEEE J.*, 1989, **QE-25,** pp. 1245–1253

24 MAGARI, K., KAWAGUCHI, H., OE, K., and FUKUDA, M.: 'Optical narrow band filters using optical amplification with distributed feedback', *IEEE J.*, 1988, **QE-24,** pp. 2178–2190

25 SHOJI, H., ARAKAWA, Y., and FUJII, Y.: 'New bistable wavelength switching device using a two-electrode distributed feedback laser', *Electron. Lett.*, 1988, **24,** pp. 888–889

26 HOEFER, W.J.R.: 'The transmmission-line matrix method — Theory and applications', *IEEE Trans.*, 1987, **MTT-35,** pp. 370–377

27 LOWERY, A.J.: 'New inline wideband dynamic semiconductor laser amplifier model', *IEEE Proc. J, Optoelectron.*, 1988, **135,** pp. 242–250

28 LOWERY, A.J.: 'A comparison between Fabry–Perot and travelling wave laser amplifiers in an 8 Gbps repeatered optical systems using a time-domain model', *J. Phys. D — Applied Phys.*, 1988, **21,** pp. S177–S179

29 LOWERY, A.J.: 'Pulse compression mechanisms in semiconductor laser amplifiers', *IEE Proc. J, Optoelectron.*, 1989, **136,** pp. 141–146

30 LOWERY, A.J.: 'Transmission-line modelling of semiconductor lasers'. PhD Thesis, University of Nottingham, May 1988

31 HENRY, C.H.: 'Performance of distributed feedback lasers designed to favor the energy gap mode', *IEEE J.*, 1985, **QE-21,** pp. 1913–1918

32 LOWERY, A.J.: 'Transmission-line modelling of semiconductor lasers: the transmission-line laser model', *Int. J. Numerical Modelling*, 1989, **2,** pp. 249–265

33 BUUS, J.: 'Dynamic single-mode operation of DFB lasers with phase shifted gratings and reflecting mirrors', *IEE Proc. J, Optoelectron.*, 1986, **133,** pp. 163–164

34 MOZER, A., HAUSSER, S., and PILKUHN, M.: 'Quantitative evaluation of gain and losses in quaternary lasers', *IEEE J.*, 1985, **QE-21,** pp. 719–725

35 WESTBROOK, L.D., 'Measurements of dg/dN and dn/dN and their dependence on photon energy in 1.5 μm InGaAsP laser diodes', *IEE Proc. J, Optoelectron.*, 1986, **133,** pp. 135–142

36 CARTLEDGE, J.C., and BURLEY, J.S.: 'The effect of laser chirping on lightwave system performance', *IEEE J.*, 1989, **LT-7,** pp. 568–573

37 CORVINI, P.J., and KOCH, T.L.: 'Computer simulation of high-bit-rate optical fiber transmission using single-frequency lasers', *IEEE J.*, 1987, **LT-5,** pp. 1591–1595